


Communication

Mid-Infrared Hollow-Core Fiber Based Flexible Longitudinal Photoacoustic Resonator for Photoacoustic Spectroscopy Gas Sensing

Zuying Xu ^{1,2,†}, Tailin Li ^{3,†}, Chaotan Sima ^{3,*} , Yanhong Long ³, Xiaohang Zhang ³, Yan Ai ³, Minzhi Hong ³, Muqi Chen ³, Botao Deng ³, Dajuan Lv ¹ and Ping Lu ³¹ State Key Laboratory of Optical Fiber and Cable Manufacture Technology (YOFC), Wuhan 430073, China² Everfoton Technologies Corporation Limited, Wuhan 430073, China³ National Engineering Research Center for Next Generation Internet Access System, School of Optical and Electronic Information, Huazhong University of Science and Technology, Wuhan 430074, China

* Correspondence: smct@hust.edu.cn

† These authors contributed equally to this work.

Abstract: Photoacoustic spectroscopy (PAS) has received extensive attention in optical gas sensing due to the advantages of high sensitivity, gas selectivity, and online detection. Here, a mid-infrared hollow-core fiber (HCF) based flexible longitudinal photoacoustic resonator for PAS-based gas sensing is proposed and theoretically demonstrated. A mid-infrared anti-resonant HCF is designed to innovatively replace the traditional metallic acoustic resonator and obtain a flexible photoacoustic cell in PAS. Optical transmission characteristics of the HCF are analyzed and discussed, achieving single mode operation with below 1 dB/m confinement loss between 3 and 8 μm and covering strong absorptions of some hydrocarbons and carbon oxides. With varied bending radii from 10 mm to 200 mm, the optical mode could be maintained in the hollow core. Based on the photoacoustic effect, generated acoustic mode distributions in the HCF-based flexible photoacoustic resonator are analyzed and compared. Results show that the PAS-based sensor has a stable and converged acoustic profile at the resonant frequency of around 16,787 Hz and a favorable linear response to light source power and gas concentration. The proposed novel photoacoustic resonator using HCF presents bring potential for advanced flexible PAS-based gas detection.

Keywords: photoacoustic spectroscopy; hollow core fiber; mid-infrared gas sensing; acoustic distribution

Citation: Xu, Z.; Li, T.; Sima, C.; Long, Y.; Zhang, X.; Ai, Y.; Hong, M.; Chen, M.; Deng, B.; Lv, D.; et al. Mid-Infrared Hollow-Core Fiber Based Flexible Longitudinal Photoacoustic Resonator for Photoacoustic Spectroscopy Gas Sensing. *Photonics* **2022**, *9*, 895. <https://doi.org/10.3390/photonics9120895>

Received: 4 November 2022

Accepted: 18 November 2022

Published: 23 November 2022

Publisher's Note: MDPI stays neutral with regard to jurisdictional claims in published maps and institutional affiliations.



Copyright: © 2022 by the authors. Licensee MDPI, Basel, Switzerland. This article is an open access article distributed under the terms and conditions of the Creative Commons Attribution (CC BY) license (<https://creativecommons.org/licenses/by/4.0/>).

1. Introduction

Photoacoustic spectroscopy (PAS) has developed rapidly in recent years in multi-component and cross-domain trace gas detection due to its zero-background acoustic detection, full-band response, and compact amplification [1,2]. Compared with direct gas absorption spectrum measurement methods, such as non-dispersive infrared (NDIR) and tunable diode laser absorption spectroscopy (TDLAS) [3,4], PAS does not require extended optical paths and superior photodetectors for improved sensitivity. It could directly enhance the photoacoustic effect by increasing the optical power and optimizing the photoacoustic resonator [5]. Conventional H-type longitudinal photoacoustic resonators were generally used [6,7]. Various modified structures were also reported and applied in photoacoustic cells [8–10]. Yin et al. developed a sub-ppb level PAS-based sensor by using a differential H-type photoacoustic resonator [9]. Gong et al. presented a T-type photoacoustic cell for ppb-level detection of CH_4 [8]. Xiao et al. proposed an ultra-sensitive all-optical PAS gas sensor with a double channel differential T-type photoacoustic resonator [10]. To be noted, the above-mentioned photoacoustic resonators are normally longitudinal and with straight cylindrical geometry. They were made from brass or stainless steel, lacking bendability and flexibility.

Since the optical absorption of gas molecules generally occurs strongly in the mid-infrared (MIR) band, hollow-core fiber (HCF), as an emerging special optical fiber with wide MIR bandwidth and efficient optical transmission, has become a hot topic in MIR gas detection [11]. The light guiding mechanism in HCF generally includes photonic band gap effect and anti-resonance effect [12,13]. Yao et al. used a hollow-core anti-resonant fiber (HC-ARF) with a length of 0.85 m as a gas chamber in TDLAS [14]. Yao et al. used tellurite HC-ARF guiding 5.26 μm light for NO detection [15]. Chen et al. reported a MIR photothermal spectroscopy ethane sensor with an HC-ARF supporting 1.55 μm and 3.348 μm [16]. Zhao et al. used a gas-filled HC-ARF to demonstrate photoacoustic Brillouin spectroscopy for C₂H₂ detection [17]. It is found that the HCF was rarely incorporated with the photoacoustic principle and could be explored.

In this paper, a flexible HCF-based photoacoustic resonator for PAS-based MIR gas detection is proposed and numerically demonstrated. The HC-ARF with low transmission loss in the MIR band is designed and simulated, and the fiber confinement loss is less than 1 dB/m within the MIR range of 3–8 μm, covering strong absorptions of some hydrocarbons and carbon oxides. The designed HCF exhibits a certain bending resistance with a 10–200 mm bending radius. When the bending radius is above 50 mm, the overall confinement loss does not increase significantly, and the transmitted light can be confined in the hollow core. The generated acoustic field distribution of the designed photoacoustic resonator is simulated and analyzed. Results show that the acoustic pressure exhibits favorable distribution around 16,787 Hz and could essentially maintain with varied bending radii in the curved photoacoustic resonator. The designed longitudinal photoacoustic cell also exhibits linear responses to light source power and gas concentration. This flexible photoacoustic resonator using HCF has great potential for advanced PAS-based optical gas sensing.

2. Structure and Principle

2.1. Hollow-Core Fiber Structure

The cross-section of the proposed HC-ARF is schematically shown in Figure 1. The main geometric factor affecting the transmission spectrum lies in the thickness of the thin-layer capillary wall. The walls of the surrounding silica tubes and the surrounding air construct the anti-resonance layer. The cladding layer of the HCF is composed of 7 silica tubes and the central hollow core is about 130 μm in diameter. The fiber cladding consists of seven identical non-contact tubes with an inner diameter of 65 μm and a thickness of 1.4 μm.

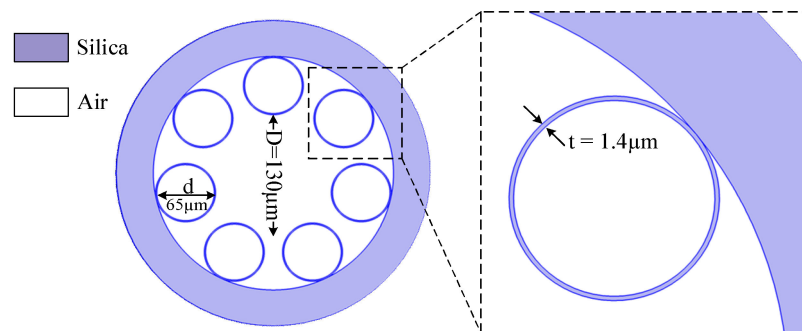


Figure 1. Cross section of the proposed HC-ARF to be applied in the photoacoustic resonator.

The cross section of the HC-ARF is divided into homogeneous subspaces that uses the finite-element method (FEM) with the perfectly matched layer (PML) boundary condition to solve Maxwell’s equations. The PML boundary condition is employed, which has been proven to be accurate and reliable in the literature [18]. The following vectorial wave equation is derived as:

$$\nabla \times \left([s]^{-1} \nabla \times \vec{E} \right) - k_0^2 n^2 [s] \vec{E} = 0 \tag{1}$$

$$[s] = \begin{bmatrix} s_y/s_x & 0 & 0 \\ 0 & s_x/s_y & 0 \\ 0 & 0 & s_x s_y \end{bmatrix} \tag{2}$$

where $k_0 = 2\pi/\lambda$ is the wave number in the vacuum and λ is the wavelength, n is the refractive index, $[s]$ is the perfectly matched layer boundary matrix, s_y and s_x are PML parameters, and E is the electronic field.

The confinement loss L is defined as [19]:

$$L = \frac{20}{\ln 10} \frac{2\pi}{\lambda} \text{Im}(n_{eff}) \tag{3}$$

where n_{eff} is the effective refractive index and λ is the optical wavelength.

Bending loss is derived from the change of effective refractive index while bending. The inner area of the fiber cross-section is squeezed, and the outside is stretched. Then the refractive index of the outside area increases and the uneven distribution of the refractive index make the modes leak easily, i.e., bending loss. The change in refractive index is defined by [13]:

$$n'(x, y) = n_0(x, y) \left(1 + \frac{x \cos \theta + y \sin \theta}{R} \right) \tag{4}$$

2.2. Photoacoustic Spectroscopy and Photoacoustic Cell

In the PAS gas sensing, gas molecules absorb optical signals and are excited to a high-energy band. After the energy is converted into heat, it returns to a low-energy band. If the incident light is frequency modulated, the heat energy will exhibit simultaneous periodic change and generate acoustic waves, to be detected by microphones. The intensity of the photoacoustic signal SPA can be simply expressed as [20]:

$$S_{PA} = K_{cell} \alpha C P_i \tag{5}$$

where K_{cell} is the cell constant of the photoacoustic cell, jointly determined by the quality factor, the volume of the photoacoustic cell and the modulation frequency, α is the absorption coefficient of the target gas, C is the gas concentration, and P_i is the optical power of the incident light.

The photoacoustic cell is an essential part where the photoacoustic effect occurs. It normally contains an acoustic resonator, two buffer volumes, optical windows, and gas inlet/outlet. In this paper, the designed HC-ARF is utilized as the flexible acoustic resonator to realize the light transmission as well as acoustic amplification simultaneously. The numerical model of the photoacoustic cell is simplified and optical windows as well as tiny gas inlet/outlet holes are ignored to facilitate numerical analysis. The established model of the flexible longitudinal photoacoustic cell is shown in Figure 2. In the photoacoustic cell, the photoacoustic resonator has a radius of 0.13 mm and a length of 10 mm. The buffer volume has a radius of 0.5 mm and a length of 5 mm.

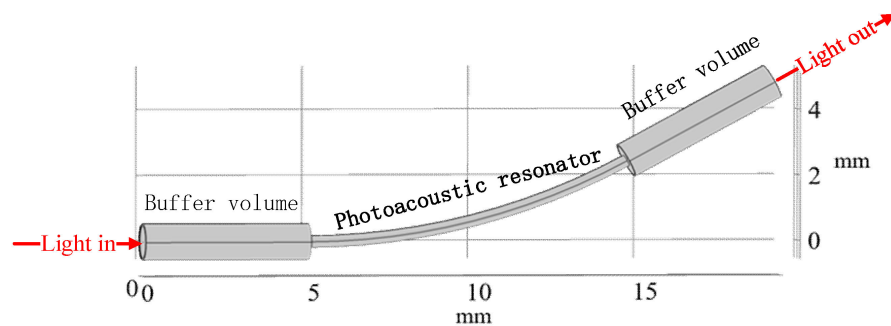


Figure 2. The proposed flexible longitudinal photoacoustic cell including a curved photoacoustic resonator and two buffer volumes.

3. Simulation and Analysis

3.1. HCF Simulation

The HCF is employed as the flexible photoacoustic resonator in PAS. Figure 3 shows the normalized optical field distribution of the fundamental mode in the proposed HCF, with the straight fiber in Figure 3a and bent fiber in Figure 3b. It is observed that the optical fields could be well confined in the central hollow core. In Figure 3b, the bending radius of the HCF is 100 mm, and the bending direction is along the horizontal axis. In this case, the optical field shifts to the horizontal side, but still stays in the core region.

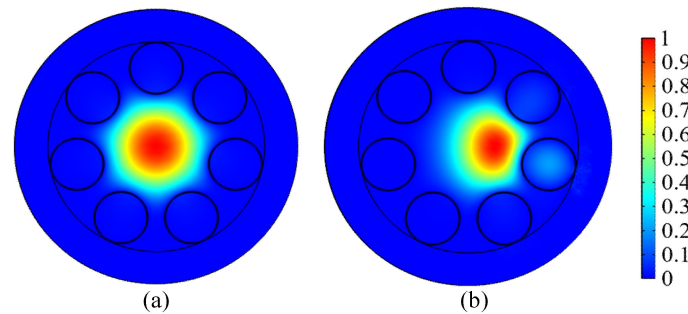


Figure 3. Normalized optical field distributions of the fundamental mode of the designed HCF: (a) straight fiber; (b) curved fiber with the bending radius of 100 mm.

The confinement loss of the HCF with orthogonal polarization states is presented in Figure 4. The fiber has a low loss (below 1 dB/m) region between 3 and 8 μm , covering strong absorptions of most hydrocarbons and carbon oxides, e.g., CO, CO₂, CH₄, C₂H₂, C₂H₄, etc. The x-polarization and y-polarization states are nearly identical with loss characteristics, indicating polarization insensitivity.

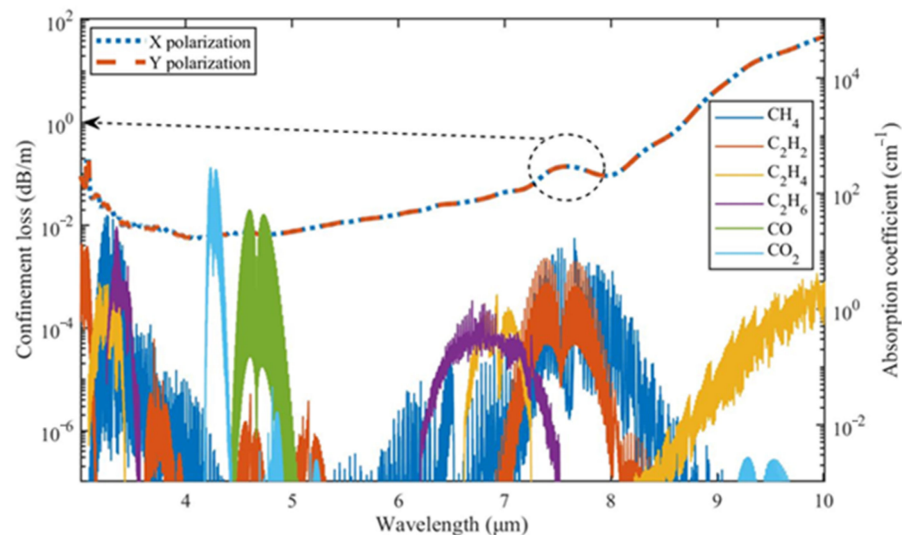


Figure 4. Confinement loss spectrum of the HCF and gas absorption spectra between 3 μm and 10 μm .

The bending loss of the HCF is also simulated and analyzed, as shown in Figure 5a. Figure 5b shows the corresponding optical mode distributions under different bending radius and wavelength. Generally, the bending loss decreases as the bending radius increases when bending radius changes from 10 mm to 200 mm. To be noted, the coupling of the core mode with the cladding mode, such as the mode fields MF 1 and MF 2, would break this tendency. The bending loss is below 20 dB/m with bending radius over 50 mm and below 1 dB/m with bending radius over 100 mm, which indicates excellent light-guiding properties of the bent HCF.

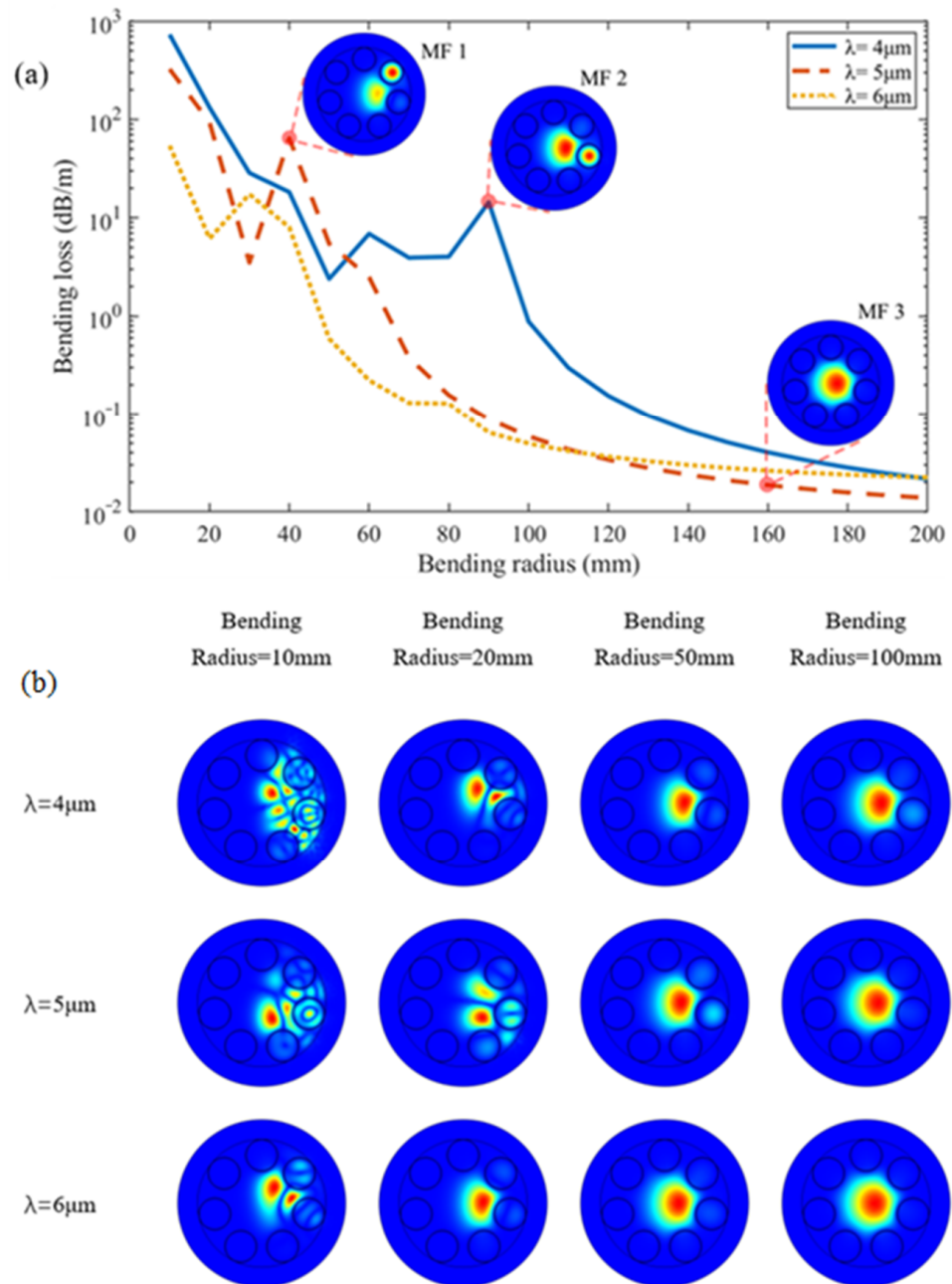


Figure 5. (a) Bending loss of the HCF with respect to bending radius when the transmission wavelength is 4 μm , 5 μm and 6 μm . Optical mode distributions for some marked points are included; (b) the corresponding optical mode distributions at wavelengths of 4 μm , 5 μm and 6 μm , when the bending radii are 10 mm, 20 mm, 50 mm and 100 mm respectively.

3.2. Photoacoustic Cell with Acoustic Analysis

The cavity structure of the photoacoustic cell has the acoustic resonant frequency and the corresponding mode profile. The acoustic mode directly manifests the pressure distribution characteristics of the cavity. The FEM was also used to solve the generated acoustic mode in the photoacoustic cell. The COMSOL Multiphysics software package was employed for simulation. The fluid material in the photoacoustic cell is defined as air, with the density of $352.761/T$. T denotes the ambient temperature (293.15 K) and the acoustic speed is set to 340 m/s. The acoustic modal simulation of the photoacoustic cell is shown in Figure 6, with the bending radius of 100 mm.

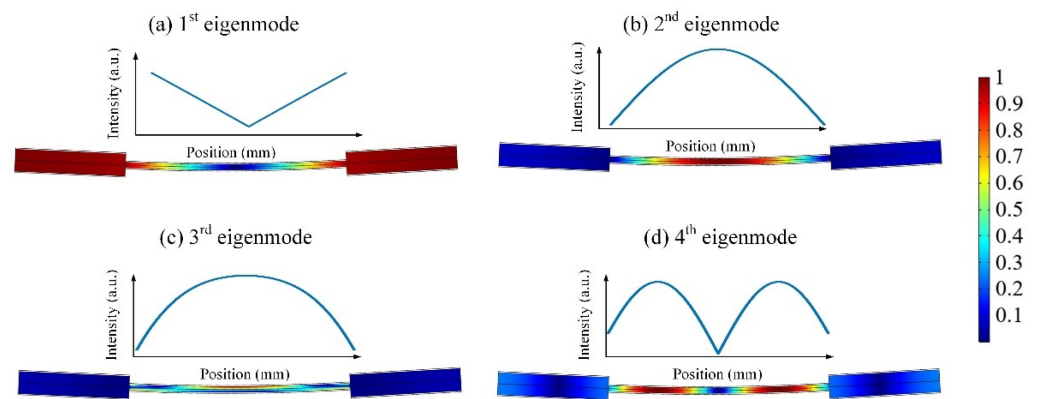


Figure 6. Calculated acoustic distribution within the photoacoustic resonator: (a) The 1st eigenmode at 2735 Hz; (b) the 2nd eigenmode at 16,787 Hz; (c) the 3rd eigenmode at 19,715 Hz; (d) the 4th eigenmode at 31,044 Hz.

It is observed from Figure 6 that the calculated 1st to 4th eigenmodes altogether exhibit longitudinal modal profiles. The colors from red to blue indicate the relative magnitude of the acoustic pressure. To clarify the acoustic pressure distribution in the photoacoustic resonator, the distributions of acoustic pressure along the central axis of the resonator with respect to varied bending radii from 10 mm to 100 mm are further analyzed. Figure 7 shows the acoustic pressure distributions along the central axis of the resonator corresponding to the four eigenmode frequencies, with the bending radius varied to 10 mm, 20 mm, 50 mm, and 100 mm. The acoustic pressure distributions of the same order eigenmodes maintain similar shapes with respect to different bending radii. The 2nd and 3rd eigenmodes both exhibit an expected parabola shapes and would be physically detectable. Considering the advanced acoustic pressure amplitude, the 2nd acoustic eigenmode at 16,787 Hz is selected in the following work.

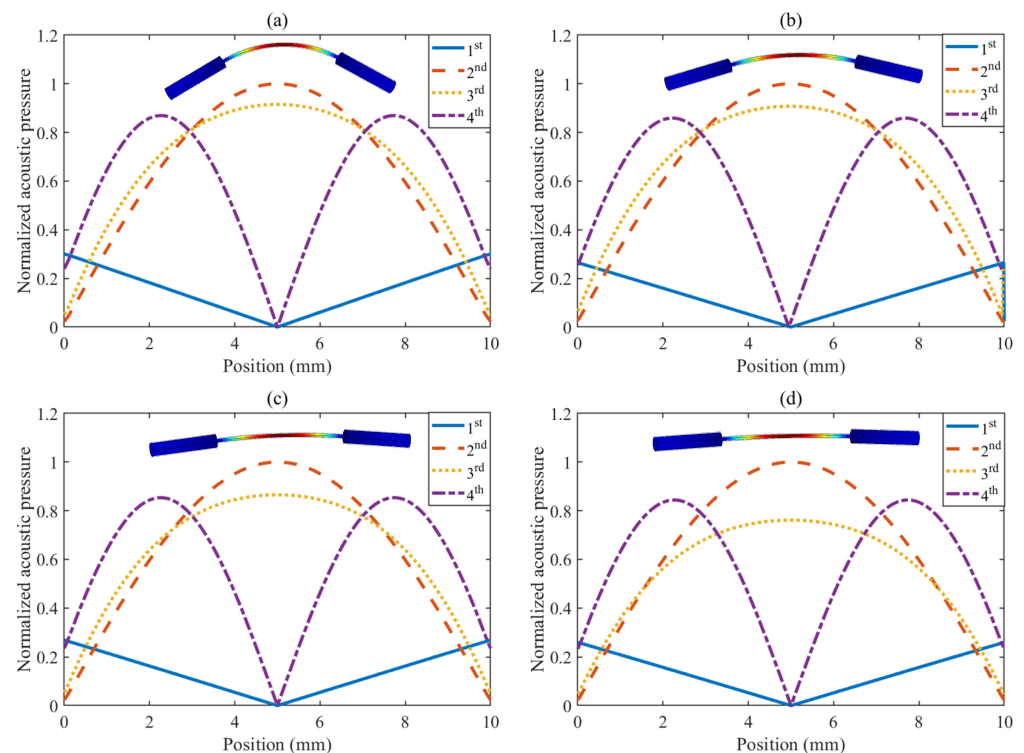


Figure 7. The acoustic modes along the HCF central axis of different eigenmodes with respect to varied bending radii: (a) 10 mm; (b) 20 mm; (c) 50 mm; (d) 100 mm.

Along with the above mentioned HCF, the 2nd acoustic eigenmode distribution at 16,787 Hz with four bending radii are further compared. Figure 8a displays the normalized acoustic pressure distribution of the four bending radii along the resonator axis. Figure 8b is the partially enlarged view of the top area in Figure 8a. The acoustic pressure basically maintains with the bending radius from 100 mm to 20 mm, and slightly decreases to about 85% at 10 mm.

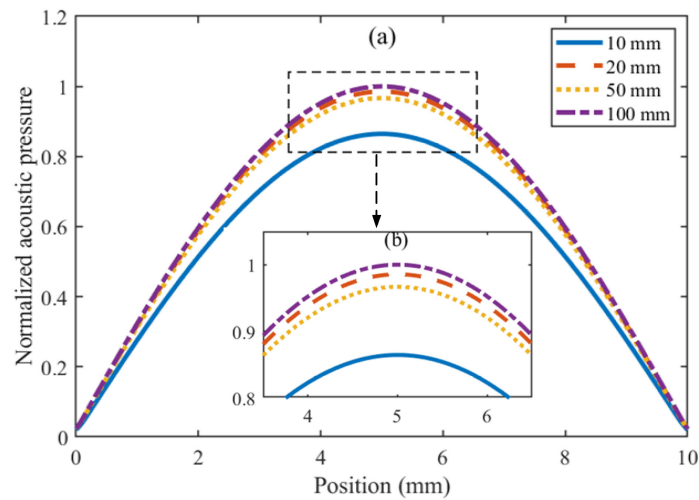


Figure 8. (a) Normalized acoustic pressure of the 2nd eigenmode within the photoacoustic resonator with varied bending radii; (b) the enlarged illustration of the central area.

To further investigate the PAS response of the proposed flexible photoacoustic cell, the heat source intensity in the PAS modal was changed, and the corresponding acoustic pressures in the center of the photoacoustic resonator with four bending radii were simulated, as shown in Figure 9. The four photoacoustic cells altogether have linear relationship with the applied heat source, with the R-square above 0.999. The detailed data of this relationship is included in Table 1. According to the photoacoustic effect and Equation (5), the heat source strength is equivalent to the multiplication of the light source power and gas concentration. Thus, it is straightforward to infer that the flexible photoacoustic cell shows a decent linear response to gas concentration and laser power.

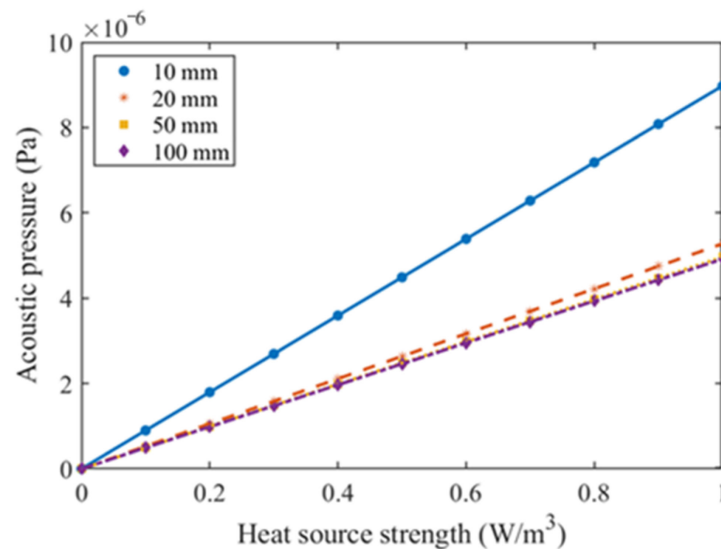


Figure 9. Variation of acoustic pressure with heat source strength at resonant frequency in four bending radius photoacoustic cells.

Table 1. Fitting equation of the acoustic pressure with respect to the heat source strength.

Bending Radius	Fitting Equations	R ²
10 mm	$y = 8.9784 \times 10^{-6}x - 9.0909 \times 10^{-12}$	1
20 mm	$y = 5.2754 \times 10^{-6}x - 9.0909 \times 10^{-12}$	1
50 mm	$y = 4.9653 \times 10^{-6}x - 9.5454 \times 10^{-12}$	1
100 mm	$y = 4.9168 \times 10^{-6}x - 5.4545 \times 10^{-12}$	1

Based on the above investigation, we further consider and discuss the practical feasibility of the proposed flexible HCF photoacoustic cell for PAS-based gas sensing. Firstly, it is well-acknowledged that the designed HC-ARF could be realized and fabricated by the current techniques for hollow core fibers [11]. In addition, micro-lens and collimators could be used for the light transmission and coupling into the proposed HCF as well as gas cells, which have been demonstrated in literatures [14–17]. In the proposed PAS system, the generated acoustic pressure signal in the photoacoustic resonator could be received and detected by a highly sensitive microphone placed in the middle of the photoacoustic resonator. With gas flow and control circuits, as well as other supporting components, the whole system could be established and realized. Practical implementation of the proposed PAS system may be presented in future publications.

4. Conclusions

In conclusion, a flexible HCF-based photoacoustic resonator for PAS-based MIR gas detection is proposed and numerically demonstrated in this paper. The HC-ARF with low transmission loss in the MIR band is designed and simulated. The confinement loss of the HCF is under 1 dB/m within the spectral range of 3–8 μm . With varied bending radii from 10 mm to 200 mm, the HCF could confine the transmitted light in the hollow core. The generated acoustic field distribution of the designed photoacoustic resonator is simulated and analyzed. Results show that the PAS has the stable and converged acoustic field distribution at the resonant frequency around 16,787 Hz and a favorable linear response to light source power and gas concentration. The proposed flexible photoacoustic resonator using HCF has great potential for advanced PAS-based optical gas sensing.

Author Contributions: Conceptualization, Z.X., B.D. and C.S.; data curation, T.L., B.D. and C.S.; writing—original draft, Z.X., T.L. and X.Z.; writing—review & editing, T.L., B.D. and C.S.; investigation, Y.L., Y.A., M.H., M.C. and B.D.; funding acquisition, Z.X., P.L., D.L. and C.S. All authors have read and agreed to the published version of the manuscript.

Funding: This work was supported by NSFC (No. 62075074), NSFC-RS Exchange Program (No. 62111530153), Science Fund for Creative Research Groups of the Nature Science Foundation of Hubei (No. 2021CFA033), and the Open Projects Foundation (No. SKLD2104) of State Key Laboratory of Optical Fiber and Cable Manufacture Technology (YOFC).

Institutional Review Board Statement: Not applicable.

Informed Consent Statement: Not applicable.

Data Availability Statement: The datasets generated during the current study are available from the corresponding author on reasonable request.

Conflicts of Interest: The authors declare that they have no conflicts of interest.

References

- Hodgkinson, J.; Tatam, R.P. Optical gas sensing: A review. *Meas. Sci. Technol.* **2013**, *24*, 012004. [[CrossRef](#)]
- Wu, H.P.; Dong, L.; Zheng, H.D.; Yu, Y.J.; Ma, W.G.; Zhang, L.; Yin, W.B.; Xiao, L.T.; Jia, S.T.; Tittel, F.K. Beat frequency quartz-enhanced photoacoustic spectroscopy for fast and calibration-free continuous trace-gas monitoring. *Nat. Commun.* **2017**, *8*, 15331. [[CrossRef](#)] [[PubMed](#)]
- Deng, B.T.; Sima, C.; Xiao, Y.F.; Wang, X.F.; Ai, Y.; Li, T.L.; Lu, P.; Liu, D.M. Modified laser scanning technique in wavelength modulation spectroscopy for advanced TDLAS gas sensing. *Opt. Laser Eng.* **2022**, *151*, 106906. [[CrossRef](#)]

4. Liu, K.; Wang, L.; Tan, T.; Wang, G.S.; Zhang, W.J.; Chen, W.D.; Gao, X.M. Highly sensitive detection of methane by near-infrared laser absorption spectroscopy using a compact dense-pattern multipass cell. *Sens. Actuat. B Chem.* **2015**, *220*, 1000–1005. [[CrossRef](#)]
5. Fu, L.; Lu, P.; Sima, C.; Zhao, J.; Pan, Y.; Li, T.; Zhang, X.; Liu, D. Small-volume highly-sensitive all-optical gas sensor using non-resonant photoacoustic spectroscopy with dual silicon cantilever optical microphones. *Photoacoustics* **2022**, *27*, 100382. [[CrossRef](#)] [[PubMed](#)]
6. Bauer, R.; Legg, T.; Mitchell, D.; Flockhart, G.M.H.; Stewart, G.; Johnstone, W.; Lengden, M. Miniaturized Photoacoustic Trace Gas Sensing Using a Raman Fiber Amplifier. *J. Lightwave Technol.* **2015**, *33*, 3773–3780. [[CrossRef](#)]
7. Ilke, M.; Bauer, R.; Lengden, M. A Calibration-Free Methodology for Resonantly Enhanced Photoacoustic Spectroscopy Using Quantum Cascade Lasers. *IEEE Sensors J.* **2020**, *20*, 10530–10538. [[CrossRef](#)]
8. Gong, Z.F.; Gao, T.L.; Mei, L.; Chen, K.; Chen, Y.W.; Zhang, B.; Peng, W.; Yu, Q.X. Ppb-level detection of methane based on an optimized T-type photoacoustic cell and a NIR diode laser. *Photoacoustics* **2021**, *21*, 100216. [[CrossRef](#)] [[PubMed](#)]
9. Yin, X.K.; Dong, L.; Wu, H.P.; Zheng, H.D.; Ma, W.G.; Zhang, L.; Yin, W.B.; Jia, S.T.; Tittel, F.K. Sub-ppb nitrogen dioxide detection with a large linear dynamic range by use of a differential photoacoustic cell and a 3.5 W blue multimode diode laser. *Sens. Actuat. B Chem.* **2017**, *247*, 329–335. [[CrossRef](#)]
10. Xiao, H.; Zhao, J.; Sima, C.; Lu, P.; Long, Y.; Ai, Y.; Zhang, W.; Pan, Y.; Zhang, J.; Liu, D. Ultra-sensitive ppb-level methane detection based on NIR all-optical photoacoustic spectroscopy by using differential fiber-optic microphones with gold-chromium composite nanomembrane. *Photoacoustics* **2022**, *26*, 100353. [[CrossRef](#)] [[PubMed](#)]
11. Yu, R.W.; Chen, Y.X.; Shui, L.L.; Xiao, L.M. Hollow-core photonic crystal fiber gas sensing. *Sensors* **2020**, *20*, 2996. [[CrossRef](#)] [[PubMed](#)]
12. Deng, B.T.; Sima, C.T.; Tan, H.Y.; Zhang, X.H.; Lian, Z.G.; Chen, G.Q.; Yu, Q.Q.; Xu, J.H.; Liu, D.M. Design of hollow core step-index antiresonant fiber with stepped refractive indices cladding. *Front. Optoelectron.* **2021**, *14*, 407–413. [[CrossRef](#)]
13. Tan, H.Y.; Sima, C.T.; Deng, B.T.; Zhang, X.H.; Chen, G.Q.; Yu, Q.Q.; Xu, J.H.; Lian, Z.G.; Liu, D.M. Design and Analysis of Ultra-Wideband Highly-Birefringent Bragg Layered Photonic Bandgap Fiber with Concave-Index Cladding. *IEEE Photon. J.* **2021**, *13*, 7100310. [[CrossRef](#)]
14. Yao, C.Y.; Xiao, L.M.; Gao, S.F.; Wang, Y.Y.; Wang, P.; Kan, R.F.; Jin, W.; Ren, W. Sub-ppm CO detection in a sub-meter-long hollow-core negative curvature fiber using absorption spectroscopy at 2.3 μ m. *Sens. Actuat. B Chem.* **2020**, *303*, 127238. [[CrossRef](#)]
15. Yao, C.Y.; Hu, M.Y.; Ventura, A.; Hayashi, J.G.; Poletti, F.; Ren, W. Tellurite Hollow-Core Antiresonant Fiber-Coupled Quantum Cascade Laser Absorption Spectroscopy. *J. Lightwave Technol.* **2021**, *39*, 5662–5668. [[CrossRef](#)]
16. Chen, F.F.; Jiang, S.L.; Jin, W.; Bao, H.H.; Ho, H.L.; Wang, C.; Gao, S.F. Ethane detection with mid-infrared hollow-core fiber photothermal spectroscopy. *Opt. Express* **2020**, *28*, 38115–38126. [[CrossRef](#)] [[PubMed](#)]
17. Zhao, Y.; Qi, Y.; Ho, H.L.; Gao, S.F.; Wang, Y.Y.; Jin, W. Photoacoustic Brillouin spectroscopy of gas-filled anti-resonant hollow-core optical fibers. *Optica* **2021**, *8*, 532–538. [[CrossRef](#)]
18. Cucinotta, A.; Selleri, S.; Vincetti, L.; Zoboli, M. Holey fiber analysis through the finite-element method. *IEEE Photon. Technol. Lett.* **2002**, *14*, 1530–1532. [[CrossRef](#)]
19. Qin, Y.; Yang, H.J.; Jiang, P.; Gui, F.J.; Caiyang, W.N.; Cao, B. Design and analysis for a bend-resistant and large-mode-area photonic crystal fiber with hybrid cladding. *Appl. Opt.* **2018**, *57*, 3976–3982. [[CrossRef](#)] [[PubMed](#)]
20. Lassen, M.; Harder, D.B.; Bruschi, A.; Nielsen, O.S.; Heikens, D.; Persijn, S.; Petersen, J.C. Photo-acoustic sensor for detection of oil contamination in compressed air systems. *Opt. Express* **2017**, *25*, 1806–1814. [[CrossRef](#)] [[PubMed](#)]